Environmental Science Advances

ROYAL SOCIETY OF CHEMISTRY

PAPER

View Article Online
View Journal | View Issue

Cite this: *Environ. Sci.: Adv.*, 2026, **5**, 900

Pyrolysis temperature dependence of Pb^{2+} removal by sewage sludge biochar: characteristic evaluation and adsorption performance

Rui Zhao,[abc] Xin Li, *[ac] Xiaoxin Jiang,[d] Guangzhi Wang,[bc] Guoren Xu,[e] Sai Qi[fg] and Guoke Zhang[fg]

Converting sewage sludge into biochar (SSB) offers a promising path for waste reduction and pollution mitigation. This study systematically investigated the effect of pyrolysis temperature (400–700 °C) on the physicochemical properties of SSB and its Pb^{2+} adsorption performance. As temperature increased, carbonization and aromaticity of SSB improved progressively. The biochar produced at 600 °C (SSB600) showed optimal characteristics—high hydrophobicity, large surface area, well-developed pores, and abundant functional groups—achieving a maximum Pb^{2+} adsorption capacity of 131 ± 10.2 mg g^{-1}. The Langmuir model best fit the adsorption isotherm data, while kinetic analysis using the Weber–Morris model indicated a multi-stage process where intraparticle diffusion was significant but not the sole rate-limiting step. SSB600 exhibited strong adsorption performance over a wide pH range (2–6) and in the presence of common competing cations (Na^+ and NO_3^-), demonstrating suitability for complex water environments. Mechanism analysis revealed that Pb^{2+} removal was driven by multiple processes: complexation (39.2%), cation exchange (38.3%), π–electron interactions (19.2%), and precipitation (3.30%). Notably, SSB600 retained over 79% of its initial capacity after eight adsorption–desorption cycles, showing excellent regenerability. It also achieved high Pb^{2+} removal (>50%) at environmentally relevant concentrations (*e.g.*, 0.5 mg L^{-1}), with environmental safety confirmed by standardized leaching tests. This work provides a pyrolysis temperature-guided synthesis strategy, fundamental mechanistic insight, and a practical viability assessment for sludge-based adsorbents. Future work should extend to pilot-scale column tests and resource recovery, supported by life-cycle analysis.

Received 4th July 2025
Accepted 11th January 2026

DOI: 10.1039/d5va00202h

rsc.li/esadvances

Environmental significance

This study aims to develop an economical, environmentally friendly, efficient and stable adsorbent from wastewater treatment waste (residual sewage sludge) to remove heavy metals from wastewater. This study has dual advantages of waste reuse and environmental remediation. It opens up a path for the sustainability of residual sludge resources and wastewater recovery.

1 Introduction

A large amount of dried sewage sludge (ss) is produced from municipal wastewater treatment plants (WWTPs) in China every year (>180 $\times 10^3$ t),[1] of which the disposition and reuse have attracted more concerns in environmental fields. Although unprocessed sewage sludge in WWTPs has been successfully applied in the remediation and agricultural soils as organic additives previously, the potential release of toxic metals (Pb, Ni, Cd, Cr, As, Hg, *etc.*) in sewage sludge may cause ecological risks.[2] Therefore, the disposition and reuse of sewage sludge from WWTPs have been a challenge because of these toxic metals. Previous studies have suggested that the pyrolysis process can stabilize toxic metals in sludge,[3,4] and the pyrolysis temperature is key to immobilize heavy metals in the biochar.[5] This process is also particularly promising because it can be

[a]*National Engineering Research Center for Safe Disposal and Resources Recovery of Sludge, Harbin Institute of Technology, Harbin 150090, China*
[b]*State Key Laboratory of Urban-rural Water Resources and Environment, Harbin Institute of Technology, Harbin 150090, China*
[c]*School of Environment, Harbin Institute of Technology, 73 Huanghe Road, Harbin 150090, China*
[d]*Water Resources and Lake Administration Bureau of Ezhou, 471 Wuchang Street, Ezhou 436000, China*
[e]*College of Resources and Environment, University of Chinese Academy of Sciences (UCAS), Beijing 100049, China*
[f]*Harbin Institute of Technology National Engineering Research Center of Water Resources Co., Ltd, Harbin 150090, China*
[g]*Guangdong Yuehai Water Investment Co., Ltd, Shenzhen 518021, China*

self-sustaining by making use of the energy derived from the combustion of the pyrolyzed bio-gas without additional energy input.[6] And the solid carbonaceous product resulting from the pyrolysis of sludge—sewage sludge biochar (SSB)—has been a considerable subject in environmental remediation due to its unique properties (*e.g.*, porous structure, abundant elemental carbon, exchangeable cations, surface adsorption sites and nutrients).[7] For example, biochar adsorption has been increasingly applied to environment remediation in both wastewater and polluted soil systems for heavy metal removal, based on a large amount of surface adsorption sites comprising carboxyl and hydroxyl groups.[8] The mechanism of biochar adsorption on heavy metal remediation mainly involves complexation with oxygen-containing functional groups on the surface, chemical precipitation with inherent minerals, ion exchange and electrostatic interactions.[7] As a result, biochar has a considerable capacity for adsorbing heavy metals.[9]

Moreover, heavy metals generally have the characteristics of degradation, difficulty, persistence and toxicity. In particular, the most typical heavy metal, Pb^{2+}, can inhibit water purification when its concentration reaches 0.100 mg L^{-1}. Thus, Pb^{2+} removal has also been a research focus due to its adverse effects on human and aquatic life.[10] Noticeably, adsorption is an efficient strategy with the advantages of simple design, specific affinity, and low cost.[11] Previous studies have suggested that biochar adsorption is a feasible strategy for efficiently removing Pb^{2+}.[12] Moreover, the results proved that the raw materials, final temperature, residence time and heating rate during pyrolysis will play crucial roles in determining the physico-chemical properties of biochar, among which the raw materials and final temperature are the key factors.[13,14] The raw material used for pyrolysis in this study was sewage sludge, which consists of organic matters (polysaccharides, protein, nucleic acids, humus, lipids and undigested organic matters), inorganic ions (CO_3^{2-}, PO_4^{3-}, SO_4^{2-}, NO_3^- *etc.*), heavy metals (Zn^{2+}, K^+, Na^+, Ca^{2+}, Mg^{2+}, *etc.*), pathogens and water.[15] These heavy metals in biochar mainly come from the biochemical immobilization from municipal wastewater, and the corrosion process of sewage pipes. Pyrolysis can reduce the risk of heavy metal release into the environment, and more importantly, previous studies have found that the final temperature can considerably affect biochar yields and its physico-chemical properties.[16] The pyrolysis temperature generally ranges from 300 to 900 °C. In contrast, a lower final pyrolysis temperature (<300 °C) will not lead to significant chemical composition change on the surface due to incomplete carbonization.[17] Studies have shown that the final pyrolysis temperature could affect the yields, ash content, pH, specific surface area, cation exchange capacity (CEC) and other characteristics of biochar,[18] as well as the element contents and heavy metal stability of biochar.[19] It is widely known that the organic components of biochar are composed of crystalline graphene sheets and randomly ordered amorphous aromatic structures. The high pyrolysis temperature can prompt high degrees of carbonization and graphitization, while the released gases and volatiles can form cracks and a porous structure. Thus, it is of great significance to explore the optimal final pyrolysis temperature for SSB preparation to improve Pb^{2+} adsorption performance. However, there is still insufficient understanding of how the final pyrolysis temperature systematically affects the multi-dimensional properties of sludge biochar (yield, ash content, pH, CEC, pore structure, surface properties, *etc.*) and its quantitative correlation with Pb^{2+} adsorption performance, as well as the dominant adsorption mechanism contribution.

In this study, sewage sludge was pyrolyzed at different final temperatures (400, 500, 600, and 700 °C) to produce a series of biochars (SSB400–700). Their physicochemical properties, including yield, ash content, elemental composition, specific surface area, pore structure, morphology, and surface chemistry, were systematically characterized. The correlation between these properties and the Pb^{2+} adsorption performance was thoroughly investigated through batch adsorption experiments and model fitting. The main objectives of this work were to: (1) elucidate the influence of pyrolysis temperature on the evolution of SSB's properties, (2) determine the optimal pyrolysis conditions for maximizing Pb^{2+} adsorption capacity and evaluate the corresponding adsorption kinetics and isotherms, (3) quantitatively decouple the contributions of different adsorption mechanisms, such as complexation, cation exchange, precipitation, and π–electron interaction, and (4) critically assess the practical viability of the optimal adsorbent, including its performance under varied pH conditions, in the presence of competing ions, its reusability over multiple cycles, and its effectiveness at environmentally relevant concentrations, complemented by an environmental safety evaluation. This study not only provided fundamental insights into the design of sludge-derived adsorbents but also demonstrated a sustainable strategy for simultaneous waste valorization and heavy metal-laden water remediation.

2 Materials and methods

2.1 Sludge pyrolysis and SSB preparation

As shown in Fig. 1, the dehydrated sludge used in this study originated from the primary sedimentation tank and the secondary sedimentation tank in a local Sewage Treatment Plant of Harbin, Heilongjiang Province. The moisture content of the sludge after dehydration was about 80.0%. The dehydrated sewage sludge was dried in an oven at 105 °C for 12 h. Then, the dried sludge was crushed using a shredder and sieved through a 60-mesh screen. A certain amount of sludge in a quartz boat was put into a pyrolysis furnace at different temperatures (400 °C, 500 °C, 600 °C, and 700 °C). The heating rate was set at 20.0 °C min^{-1}, and the heating processes were maintained for 2 h. The nitrogen flow rate was controlled at 0.100 m^3 min^{-1} as a protective gas. After the pyrolysis furnace cooled down, the produced sludge biochar was collected and marked as SSB400, SSB500, SSB600, and SSB700, respectively, for further experiments.

2.2 The characteristic evaluation of SSB

2.2.1 Thermogravimetry, yields, ash contents, pH, and elemental analysis. The thermogravimetric analysis (TGA) of

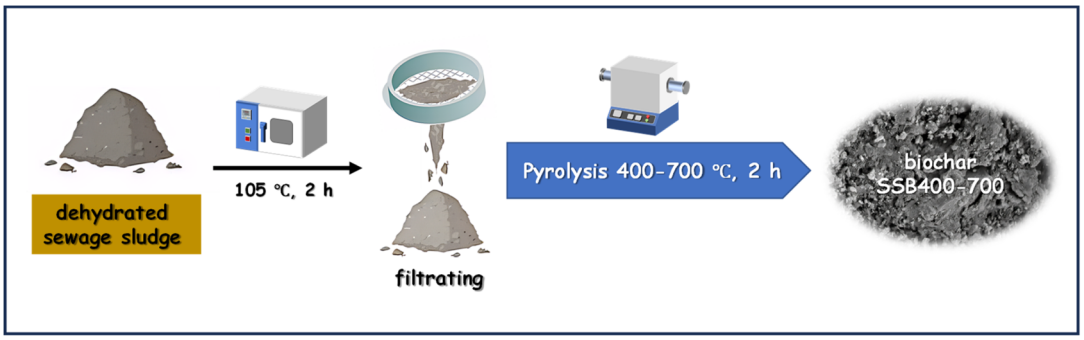

Fig. 1 The pyrolysis process of sewage sludge for preparing SSB400–700 (filtering: 60 mesh; pyrolysis rate: 20.0 °C min^{-1}; gas atmosphere: N_2, 0.100 m^3 min^{-1}).

SSB was performed by using a thermogravimetric analyzer (TG/DSC3+, Mettler Toledo) for studying mass changes at different final pyrolysis temperatures. The detection temperature range was 30.0–830 °C, and the heating rate was set at 10.0 °C min^{-1}, with N_2 used as the gas atmosphere. The yields of SSB were calculated as the ratio between the product mass after pyrolysis at different final pyrolysis temperatures and the raw sewage sludge mass (20.0 g). The ash contents of SSB (1.00 g) were measured by weighing the residual cooled solid mass after pyrolysis under open conditions in a muffle furnace at 750 °C for 4 h. The pH of SSB (1.00 ± 0.02 g) was obtained by mixing with 2.00 mL deionized water after equilibration for 24 h at 25.0 °C. The elemental analysis of SSB was performed using an elemental analyzer (UNICUBE, Elementar, Germany) for the determination of C, H, O, and N in SSB (200 mesh).

2.2.2 Water contact angles, SEM-EDS, and BET analysis. The water contact angles (WCAs) on the surface of the biochar pyrolyzed from different raw materials (ss, corn straw, and vinasse) under the same pyrolysis conditions (final pyrolysis temperature: 600 °C) were measured using a dynamic contact angle analyzer (DCA-322, Thermo Cahn, USA). Meanwhile, the surface energy of SSB600 was analyzed using the Fowkes model.[20] And the surface morphology of SSB was observed by scanning electron microscopy (SEM, ZEISS Sigma 500, UK) with an extraction voltage of 3.86 kV, and the surface elemental composition was also characterized using an energy dispersive spectrometer (EDS, X – Max 50, Oxford). Simultaneously, the Brunauer–Emmett–Teller (BET, Quadrasorb SI-MP, Quantachrome, USA) method was used to measure the specific surface area and pore size distribution of SSB.[21] The SSB samples were pretreated at 150 °C for 8 h, and N_2 was used as the gas atmosphere.

2.2.3 FT-IR and Raman analysis. A Fourier transform infrared spectrometer (FT-IR) (Specturm One B, PerkinElmer) was used to characterize the functional groups on the surface of SSB. The samples and KBr were mixed and ground in an agate mortar to prepare pellets, with a mass ratio of 1 : 200. The Raman spectral analysis was performed using a Raman spectrometer (LabRAM HR Evolution, Horiba, Japan). The SSB samples were evenly placed on a slide; the emission wavelength of the laser was 533 nm, equipped with an objective lens (50×), with a power of 10 mW, a detection time of 5 s, and 2 cycles.

2.2.4 Cation exchange capacity analysis. The cation exchange capacity (CEC) of biochar was measured by the $BaCl_2$–H_2SO_4 method.[22] Specifically, the biochar (1.00 g) was mixed with $BaCl_2$ solution (20.0 mL, AR), centrifuged at 3.00 × 10^3 rpm for 10 min, and this step was repeated twice. Then, H_2SO_4 (0.100 mol L^{-1}, 25.0 mL, AR) was added to the mixture for 20 min. After complete reaction, the supernatant (10.0 mL) was titrated with standard NaOH solution (AR), and the CEC of biochar was obtained by measuring the consumption of H_2SO_4.

2.2.5 The leaching risk evaluation of SSB. For extracting the dissolved organic matter (DOM), SSB600 was mixed with deionized water in a 1 : 10 (w: v) ratio and placed in a constant temperature shaker. It was shaken at 180 rpm for 24 h. Then, the mixture was filtered, and the obtained filtrate was filtered through a 0.45 μm filter membrane and labeled as DOM600 for further experiments. The heavy metals in DOM600 were detected by inductively coupled plasma-mass spectrometry (ICP-MS, Agilent 7700e, USA) after diluting with (1% v/v) HNO_3. The detailed organic matter composition of DOM in SSB600 was identified by pyrolysis gas chromatography-mass spectrometry (Py-GCMS, Agilent 1260/6120, USA) and liquid chromatography-mass spectrometry (LC-MS, Agilent 5977C GC/MSD, USA). The luminescence inhibition experiment of *Vibrio fischeri* was studied by the Microtox method. First, the freeze-dried *Vibrio fischeri* powder in the reagent vial was equilibrated at 25 °C for 15 min. Then, the NaCl solution (0.850%, 0.500 mL) was added to the *Vibrio fischeri* suspension and mixed at 25 °C for 15 min to maintain the same salinity level for each sample. Subsequently, the treated DOM solution was mixed evenly with 5.00 × 10^{-2} mL of *Vibrio fischeri* – NaCl solution in a clean test tube and incubated at 25 °C for 15 min. The fluorescence intensity of *Vibrio fischeri* was measured using a Microtox biotoxicity analyzer. The fluorescence intensity of *Vibrio fischeri* in the NaCl solution was used as the negative control blank (100% luminescence). Additionally, 3,5-dichlorophenol was used as a toxicity reference substance to evaluate its effect on the fluorescence intensity of *Vibrio fischeri* at different concentrations (0.00, 2.00, 4.00, 6.00, 8.00, and 10.0 mg L^{-1}), and the luminescence inhibition efficiency (%) = (fluorescence value of NaCl solution − fluorescence value of DOM solution)/fluorescence value of NaCl solution × 100.

2.3 Batch assays of SSB adsorption performance on Pb^{2+} adsorption

The diverse SSB samples (SSB400–700, 20.0 g) and Pb^{2+} solutions (initial concentration: 0.500, 1.00, 10.0, 20.0, 50.0, 100, 150, 200, 250, 300 mg L^{-1}, 20.0 mL) were mixed in PET bottles (50.0 mL). The electrolyte solution was $NaNO_3$ (10.0 μmol L^{-1}), and the initial pH was adjusted to 5.00 ± 0.010. The PET bottles were oscillated at 220 rpm at 25.0 °C for 24 h. After the reaction, the samples (1.50 mL) were picked up from the PET bottles at fixed times, immediately followed by centrifugation at 3.00 × 10^3 rpm, filtration through a 0.220 μm filter membrane, and storage at 4.00 °C. Then, the supernatant was diluted with (1.00% v/v) HNO_3 (AR) and the Pb^{2+} concentration was finally determined using an Inductively Coupled Plasma Optical Emission Spectrometer (ICP-OES, 5300DV, PerkinElmer, USA).[23] The results present averages of experiments in triplicate, and error bars represent standard deviations. In further recycled experiments, 0.1 mol L^{-1} HNO_3 was utilized as the regenerant, and after achieving Pb^{2+} adsorption saturation, eight consecutive adsorption–regeneration cycles during Pb^{2+} adsorption by SSB600 were performed.

2.4 The fitting of the Langmuir, Freundlich, and Weber–Morris intraparticle diffusion adsorption models

A series of different initial concentration Pb^{2+} solutions (20.0, 50.0, 100, 150, 200, 250, 300 mg L^{-1}) were adjusted to pH 5.00 ± 0.10, and then mixed with SSB400–700 at 220 rpm and 25.0 °C for 24 h. Eventually, the water samples were filtered through a 0.220 μm filtration membrane, and the Pb^{2+} concentration was measured by ICP-OES.

The Langmuir isothermal adsorption model was generally utilized to describe monolayer adsorption on the surface of adsorbents. The Langmuir isothermal adsorption model is expressed as follows eqn (1):[24]

$$\frac{C_e}{Q_e} = \frac{1}{Q_{max}}C_e + \frac{1}{Q_{max}k_L} \quad (1)$$

The Freundlich isothermal adsorption model was used to describe the process of heterogeneous adsorption on the surface of adsorbents. The equation is expressed as follows eqn (2):[25]

$$\ln Q_e = \ln k_f + \frac{1}{n}\ln C_e \quad (2)$$

where k_L – Langmuir constant (L mg^{-1}), k_f – Freundlich constant ($mg^{1-1/n}/(L^{1/n}\ g)$), Q_e – adsorption capacity at equilibrium (mg g^{-1}), Q_{max} – maximum adsorption capacity (mg g^{-1}), C_e – solution concentration at equilibrium (mg L^{-1}), and $1/n$ – heterogeneous factor.

The Weber–Morris intraparticle diffusion model was particularly useful for identifying whether the transport of Pb^{2+} within the pores of SSB600 controlled the adsorption rate. The model is expressed as follows eqn (3):[26]

$$q_t = kt^{1/2} + b \quad (3)$$

where q_t – adsorption amount at time 't' (mg g^{-1}), k – particle internal diffusion constant (mg (g $h^{1/2}$)), and b – intercept.

2.5 The experiment of adsorption contribution

First, SSB600 was pre-treated for demineralization. SSB600 (1.00 ± 0.01 g) was weighed and mixed with HCl (1.00 mol L^{-1}, 50.0 mL). After fully removing the minerals in SSB600, the samples were collected by centrifugation from the solid–liquid mixture (repeated three times) and washed until the pH of the filtrate no longer changed. The Pb^{2+} solution was mixed with unmined and mined SSB600 (20.0 mL) for adsorption, respectively. After the adsorption reaction was completed, the concentrations of K^+, Ca^{2+}, Mg^{2+}, Mn^{2+} and Pb^{2+} were detected. The formula for calculating the adsorption amount of the specific adsorption mechanism is shown as follows:

$$q_1 = q_{bc} - q_{bd}Y \quad (4)$$

where q_1 – the amount of Pb^{2+} adsorption attributed to the precipitation effect, q_{bc} – the amount of Pb^{2+} adsorption by unmined SSB600 (mg g^{-1}), q_{bd} – the amount of Pb^{2+} adsorption by mined SSB600 (mg g^{-1}), and Y – correction factor.

$$q_2 = \frac{1}{2}q_K + q_{Ca} + q_{Mg} + q_{Mn} \quad (5)$$

where q_2 – the amount of Pb^{2+} adsorption attributed to the cation exchange effect (mg g^{-1}), q_k – the amount of K^+ release during Pb^{2+} adsorption by unmined SSB600 (mg g^{-1}), q_{Ca} – the amount of Ca^{2+} release during Pb^{2+} adsorption by unmined SSB600 (mg g^{-1}), q_{Mg} – the amount of Mg^{2+} release during Pb^{2+} adsorption by unmined SSB600 (mg g^{-1}), and q_{Mn} – the amount of Mn^{2+} release during Pb^{2+} adsorption by unmined SSB600 (mg g^{-1}).

$$q_3 = q_H Y \quad (6)$$

where q_3 – the amount of Pb^{2+} adsorption attributed to the complexation effect (mg g^{-1}), and q_H – the amount of K^+ release during Pb^{2+} adsorption by unmined SSB600 (mg g^{-1}).

$$q_4 = q_{bc} - q_1 - q_2 - q_3 \quad (7)$$

where q_4 – the amount of Pb^{2+} adsorption attributed to π–electron coordination.

3 Results and discussion

3.1 Effect of final pyrolysis temperature on Pb^{2+} adsorption performance

A series of different final pyrolysis temperatures (400 °C, 500 °C, 600 °C, and 700 °C) were set for investigating the adsorption performance of SSB for Pb^{2+} removal (initial Pb^{2+} concentration: 0.500–300 mg L^{-1}). And the SSB samples pyrolyzed at 400–700 °C were marked as SSB400, SSB500, SSB600, and SSB700, respectively. As the initial Pb^{2+} concentration increased, the Pb^{2+} adsorption efficiencies declined gradually, and the corresponding adsorption efficiencies of SSB400–SSB700 were 16.4–63.2%, 21.7–64.3%, 26.9–70.1%, and 28.8–70.2% respectively. The higher Pb^{2+} adsorption efficiency was shown between 600

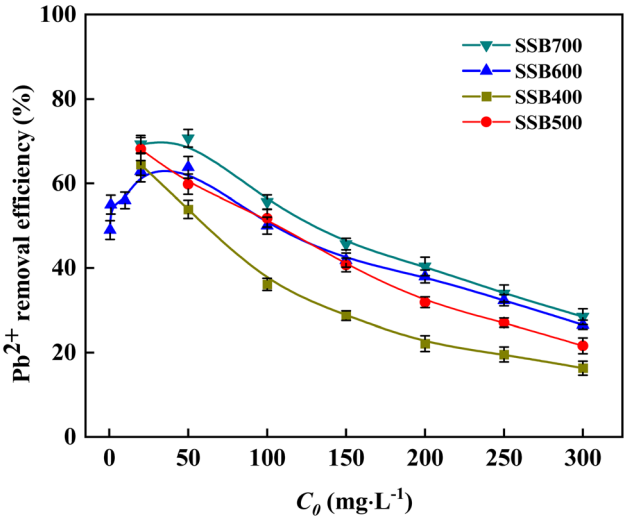

Fig. 2 Pb^{2+} adsorption efficiencies of SSB400–700 (initial Pb^{2+} concentration: 0.500, 1.00, 10.0, 20.0, 50.0, 100, 150, 200, 250, 300 mg L^{-1}; adsorbent dosage: 1.00 g L^{-1}, pH: 5.00 ± 0.1, 25.0 °C; reaction time: 24 h).

and 700 °C by SSB600 or SSB700 (Fig. 2). Sequentially, based on consideration of energy savings, 600 °C was chosen to be a better final pyrolysis temperature for SSB production and SSB600 was utilized to remove Pb^{2+} and study the Pb^{2+} adsorption process by SSB in the following experiments. For Pb^{2+} trace concentration removal, the Pb^{2+} removal capacity was investigated at low initial Pb^{2+} concentration (0.500, 1.00, and 10.0 mg L^{-1}) by optimal SSB600. The stable removal efficiency was kept at 50%, 55%, and 56%, respectively, suggesting effective Pb^{2+} removal by SSB. Furthermore, the adsorption capacity of biochar for heavy metals under varying pyrolysis conditions was strongly influenced by its functional groups and specific surface area.[21] The ability of biochar to adsorb Pb^{2+} was likely due to synergistic interactions among morphological characteristics, CEC, BET surface area, surface functional groups and the release potential elements (P, Mg, *etc.*).[27] Therefore, Pb^{2+} adsorption by SSB was further studied by charactering SSB surface properties.

Considering the significant influence of pH fluctuations and co-existing ions on Pb^{2+} adsorption in actual wastewater, the amount of Pb^{2+} adsorbed by SSB600 at different initial pH values (2.00–6.00) and ionic strengths (Na^+, NO_3^-) is further discussed in Fig. S1. It was shown that the adsorption capacity of SSB600 was significantly reduced at pH < 4.00 by 45.9% on average, which was mainly due to the competition between the high concentration of H^+ and Pb^{2+} for adsorption sites, resulting in the inhibition of the protonated surface for binding of metal ions. In the pH 5.00–6.00 range, the Pb^{2+} adsorption performance reached a peak and tended to be stable, indicating that the material had a stable adsorption capacity. Therefore, the optimal experimental pH was selected as 5.00 ± 0.10. Based on the preliminary experiments and reported studies, the optimal Pb^{2+} adsorption pH range was between 5.00 and 6.00, where Pb^{2+} exhibited a low degree of hydrolysis and strong complexation with surface functional groups (such as carboxyl and hydroxyl groups). Simultaneously, for discussing the compatibility with actual pH fluctuations in wastewater, it was fully agreed that the pH of actual wastewater may be much lower than 5.00, while some ambient water bodies may be close to neutral or weakly alkaline. Thus, SSB was expected to exhibit good adsorption performance (84.2% on average) when the pH was between 5.00 and 6.00, and if the pH was consistently below 4, the pH would be adjusted by pretreatment or the development of modified materials with more acid tolerance should be considered. If the pH was above 6, it should be noted that Pb^{2+} may gradually form hydroxide precipitates, and the adsorption mechanism will change from complexation to precipitation synergy, which would affect the final Pb^{2+} removal performance in practical applications. Regarding the effect of different ionic strengths ($NaNO_3$ concentration: 1.00×10^{-3}, 1.00×10^{-2}, 1.00×10^{-1} mol L^{-1}) on Pb^{2+} adsorption, the effect was more obvious at high ionic strength, which had an increasing trend of Pb^{2+} adsorption capacity with increasing ionic strength. It was indicated that pH and ionic strength may jointly affect the Pb^{2+} adsorption capacity in practical wastewater with complex ionic composition. And the equilibrium pH values after adsorption were 2.53–8.52 at pH 2–6. It was suggested that alkaline conditions gradually formed during the Pb^{2+} adsorption

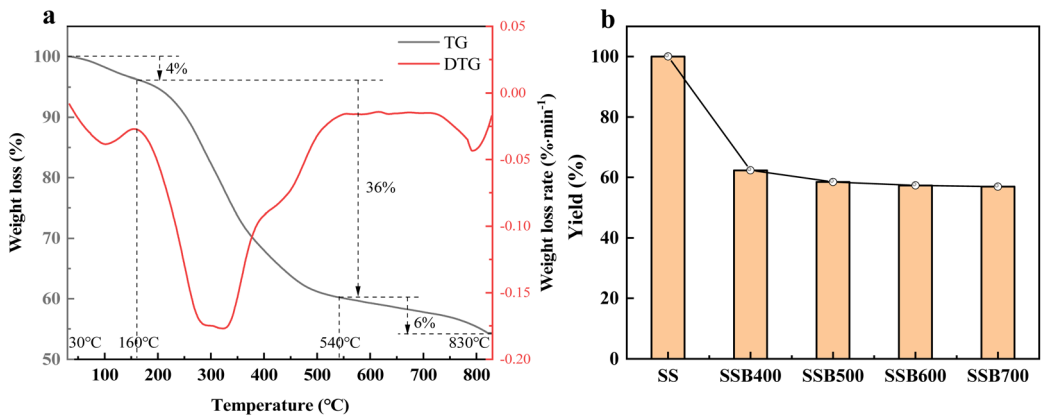

Fig. 3 Thermogravimetric analysis curve of the raw sewage sludge (ss) (instrument model: TG/DSC3+; heating rate: 10 °C min^{-1} under a N_2 atmosphere) (a); yields of ss and SSB400–700 °C (yield calculation based on 20.0 g of ss) (b).

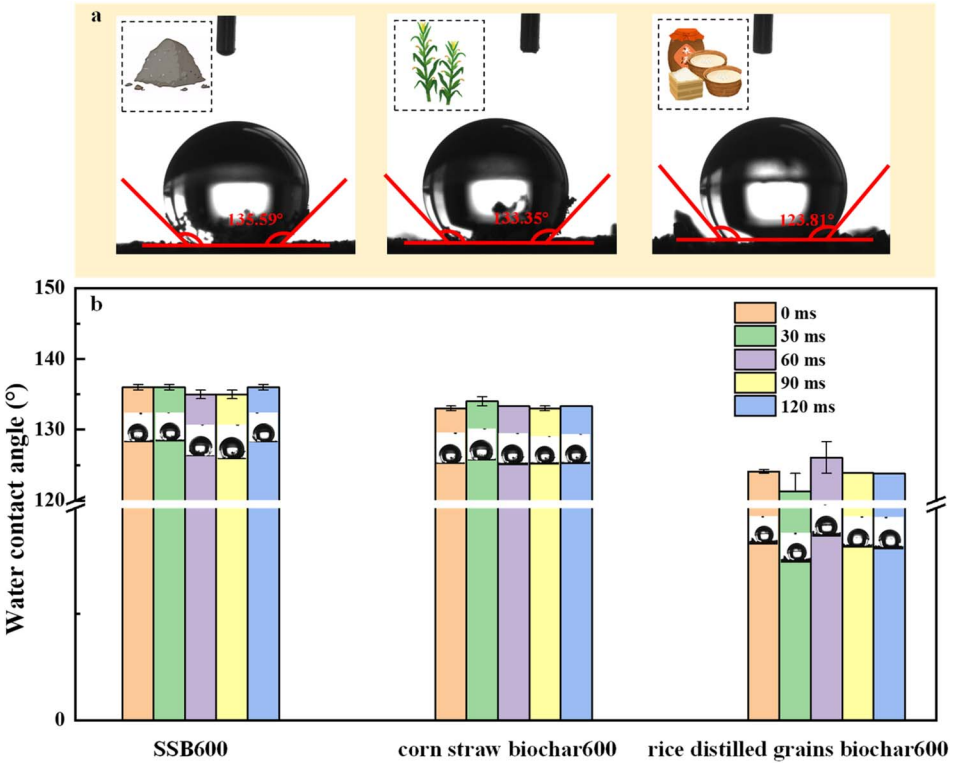

Fig. 4 Water contact angles of SSB600 and two kinds of biochar pyrolyzed at 600 °C from other raw materials (corn straw biochar 600 and vinasse biochar 600): average water contact angle (a); change in dynamic water contact angle within 120 ms (b). Test liquid: deionized water; droplet volume: 2 μL.

process, implying the probable lead-containing hydroxide production.

3.2 General characteristics of SSB

As shown in Fig. 3, the weight loss of ss during the pyrolysis process occurred in three stages within the temperature range of 30.0–830 °C: 30.0–160 °C, 160–540 °C, and 540–830 °C. In the three stages, the weight loss was 4.00%, 36.0%, and 6.00%, respectively, with the maximum weight loss occurring at 338 °C (Fig. 3a). This was consistent with the yield reduction observed with increasing pyrolysis temperature (Fig. 3b). In the first stage, the weight loss was mainly due to water evaporation. During the 160–540 °C period, the mass loss increased rapidly, which may be attributed to the condensation of aromatic compounds, volatilization and decomposition of inorganic salts, and the chain reactions of other complex compounds.[27] Simultaneously, redox reactions probably occurred, produced by the functional groups such as quinonyl, phenolic hydroxyl group, *etc.*[28] And in the 540–830 °C stage, the weight loss gradually stabilized, mainly due to the residual decomposition of organic and inorganic matters in the ss. Based on the gradual decomposition of the substances in the sludge, the yields of SSB400–700 declined steadily from 62.3% to 56.9%, respectively, with increasing pyrolysis temperature (Fig. 3b). Importantly, the more volatile components will eventually be converted into gas and liquid products as the final pyrolysis temperature improvement,[29] resulting in a decreased reduction rate of biochar yields. This was in agreement with other studies.[30] Compared with biochar pyrolyzed from other raw biomass, it can be found that the yields of fiber, pigment, and lignin of biochar from agricultural biomass (*e.g.* corn straw biochar, rice straw biochar, vinasse biochar, rape straw biochar, peanut shell biochar, and coffee residue biochar) were usually 30.0–55.0% (Table S1). The yields of SSB were higher than those pyrolyzed from agricultural biomass, which may be due to more inorganic salts in sewage sludge.[31]

Simultaneously, the super wettability of SSB600 by dynamic water contact angle (WCA) measurements was evaluated and compared with other biochar pyrolyzed from diverse raw materials. As shown in Fig. 4a, the average WCA of SSB600 was 136° (>90.0°), larger than that of corn straw biochar 600 (133°) and vinasse biochar 600 (124°), exhibiting stronger hydrophobicity compared with biochar pyrolyzed from lignin and cellulose biomass. And according to the Fowkes model analysis, SSB600 possessed a larger polar surface energy (4.72 mN m^{-1}) than its non-polar component (1.48 mN m^{-1}), which also proved the strong hydrophobicity of SSB. During the dynamic

Table 1 The ash content, pH, and CEC of ss and SSB400–700

	ss	SSB400	SSB500	SSB600	SSB700
Ash content	44.2%	70.1%	73.2%	75.7%	80.7%
pH	4.45	5.58	7.51	8.9	8.72
CEC (cmol kg^{-1})	16.7	3.42	3.67	4.00	2.93

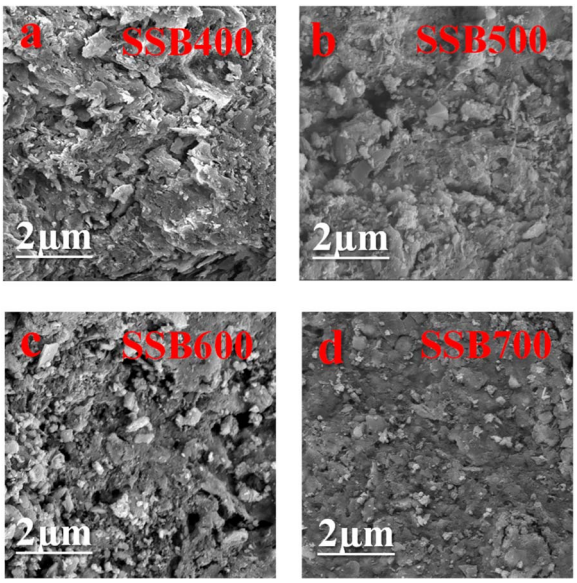

Fig. 5 Scanning electron microscopy (SEM) images of SSB prepared at different pyrolysis temperatures (400–700 °C) at 2000× magnification, accelerating voltage = 3.86 kV: (a) SSB400, (b) SSB500, (c) SSB600, and (d) SSB700.

process within 120 ms, there was a constant WCA of SSB600 than that of other two biochar products (Fig. 4b), which showed a porous structure and stable surface chemical properties.

Except for yields, the final pyrolysis temperature also affected ash contents, pH and cation exchange capacity (CEC) of the biochar (Table 1).[32] The percentage of ash contents increased significantly by 25.9%, 29.0%, 31.6%, and 36.5% with increasing final pyrolysis temperature from 400 to 700 °C. A similar phenomenon was consistent with previous studies by Yuan *et al.*[33] and Wang *et al.*[34] Compared to the initial ash contents of raw sewage sludge (44.2%), an increase in ash contents (>70.1%) was observed in SSB, and there was an influent positive relation between pyrolysis temperature and the ash contents of the biochar. This may suggest that a majority of inorganic components were retained in the biochar, along with the decomposition of organic matter in the raw sludge biomass during the pyrolysis process simultaneously.[35]

After the pyrolysis process, the pH of SSB was usually neutral and become alkaline, corresponding to increasing pH values of 5.58, 7.51, 8.90, and 8.72 with increasing final pyrolysis temperature (400–700 °C) (Table 1). Significantly, there was an important correlation between ash contents and the pH of biochar pyrolyzed at 400–700 °C, which indicated that the ash content may be a major factor contributing to the alkaline surface of the biochar.[36] There were also two main explanations the alkaline properties of SSB: (i) biochar had diverse alkaline components (*e.g.*, hydroxides or oxides of heavy metals) that could be released into the wastewater as soluble substances,[37] which was consistent with the ash content improvement of SSB400–700 (Table 1); (ii) there were highly aromatic functional groups on the surface of biochar (*i.e.*, phenolic–OH, alcoholic–OH, and –COOH),[38] which could also have an influent impact on pH of the biochar.[39] And it has proved that the removal efficiency of Pb^{2+} adsorbed by SSB increased with the increasing pH value (Fig. 2). The Pb^{2+} adsorption capacity was increased because of more OH^- concentrations, which reacted with Pb^{2+} to precipitate $Pb(OH)_2$. On the other hand, the competition between the protons and cations such as K^+ and Ca^{2+}, released by SSB into the solution would also lead to decreased Pb^{2+} adsorption by the complexation effect at lower pH.[40]

The CEC could reflect the biochar ability to retain cations, which was indicated by the surface negative charge. The ss had a CEC value of 16.7 cmol kg^{-1}. And the CEC values of SSB400–700 were 3.42 cmol kg^{-1}, 3.67 cmol kg^{-1}, 4.00 cmol kg^{-1} and 2.93 cmol kg^{-1}, respectively (Table 1). It could be observed that there was a slight increase followed by a decrease in CEC value of SSB, among which SSB600 exhibited the highest value as the final pyrolysis temperature increases. Generally, higher pyrolysis temperature could result in higher CEC values. This trend in CEC change aligned with that observed for functional groups based on temperature.[8] With increasing pyrolysis temperature, there was a rise in pH, which promoted dissociation of functional groups (–COOH and –OH) present on the biochar surface. Thus, more negative charges remained on it and CEC increased, which facilitated cation exchange between SSB and cations ultimately. These findings were consistent with pH variations for SSB and Pb^{2+} adsorption performance presented in Table 1.[41,42]

For studying the surface structure, scanning electron microscopy (SEM) was utilized to determine how the surface morphology changed during conversion of sludge into biochar with increasing pyrolysis temperature (Fig. 5). The surface morphology and porous structure of the biochar developed gradually as the pyrolysis temperature increased. SSB400 (Fig. 5a) exhibited the structure of resembling fish scale bundles of inorganic components. As the pyrolysis temperature increased, SSB500 exhibited a more porous surface, while SSB600 and SSB700 appeared to contain more micropores but exhibited a less rough biochar surface. The changes in texture continued, as revealed by the rougher and more porous surface; SSB500–700 were adhered with inorganic components irregularly to both the outer surface and the internal pores (Fig. 5b–d). The gray particulate matter consisted of C, O, Fe and Mn elements based on mapping analysis of SSB600, as shown in

Table 2 The BET surface area and pore size distribution of SSB400–700

	ss	SSB400	SSB500	SSB600	SSB700
The surface area ($m^2\ g^{-1}$)	7.30	17.6	21.1	22.4	22.8
Average pore size (nm)	21.1	18.7	18.5	18.9	18.6
Total pore volume ($cm^3\ g^{-1}$)	4.19×10^{-2}	7.63×10^{-2}	7.79×10^{-2}	8.33×10^{-2}	8.34×10^{-2}

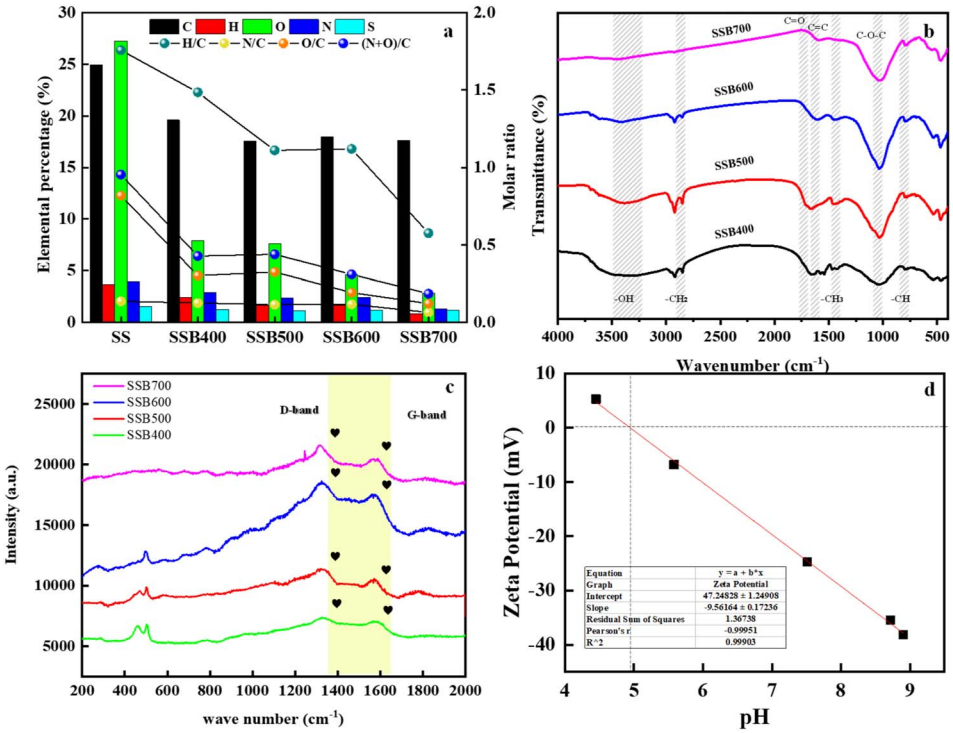

Fig. 6 Comprehensive characterization of raw sewage sludge (ss) and SSB400–700: elemental percentage (C, H, O, N, and S) and molar ratios (samples size: 200 mesh) (a); FT-IR spectra, (sample/KBr mass ratio of 1 : 200; wavenumber range: 400–4000 cm^{-1}) (b); Raman spectra (laser wavelength = 533 nm, power = 10 mW, acquisition time = 5 s, 2 accumulations) (c); zeta potential (measured in 1.00 × 10^{-2} mol L^{-1} $NaNO_3$ electrolyte) (d).

Fig. S2, and the micropores could provide abundant surface area for the attachment and adsorption of Pb^{2+}.[43,44]

As displayed in Table 2, this was corroborated by the data of the surface area of ss and SSB400–700. The surface area and the total volume of sewage sludge increased markedly from 7.30 m^2 g^{-1} and 4.19 × 10^{-2} cm^3 g^{-1} to 17.6 m^2 g^{-1} and 7.63 × 10^{-2} cm^3 g^{-1} (SSB400) after pyrolysis, while the average pore size decreased from 21.1 nm to 18.7 nm. And as the pyrolysis temperature increased (400–700 °C), the surface area and the total volume also increased gradually from 17.6 m^2 g^{-1} and 7.63 × 10^{-2} cm^3 g^{-1} to 22.8 m^2 g^{-1} and 8.37 × 10^{-2} cm^3 g^{-1}. This suggested that the interactions among components of the sewage sludge would affect the pyrolysis process of the various constituents of sludge and result in the increase of SSB heterogeneity.

As shown in Fig. S3, the adsorption/desorption isotherms of ss and SSB400–700 reflected the inherent porous structure of the materials. Both ss and SSB exhibited similar shapes in adsorption/desorption isotherms, corresponding to Type IV adsorption isotherms with H3 hysteresis loop formation, which indicated a well-developed mesoporous structure within ss and SSB400–700. As evident from these isotherms, an increase in pyrolysis temperature led to augmentation of the specific surface area of ss and SSB400–700. When pressure (P/P_0) approached to 1.00, a rapid increment can be observed in SSB400–700 adsorption behavior, which further indicated their abundant mesoporous structure. Typically, the average pore sizes of ss and SSB400–700 predominantly fell within the mesoporous range between 18.5 nm and 21.1 nm (Table 2), which affirmed the micropore-trapping effect of SSB during Pb^{2+} adsorption.

The specific surface area, average pore size, and total pore volume of original sewage sludge (ss) were 7.30 m^2 g^{-1}, 21.1 nm, and 4.19 × 10^{-2} cm^3 g^{-1} respectively (Table 2). Generally, the specific surface area and total pore volume of the biochar were increased with the increase of final pyrolysis temperature.[45] With increasing final pyrolysis temperature from 400–700 °C, the total pore volume of SSB400–700 increased from 7.63 × 10^{-2} cm^3 g^{-1} to 8.34 × 10^{-2} cm^3 g^{-1}, while the specific surface area increased from 17.6 m^2 g^{-1} to 22.8 m^2 g^{-1}. The increase in total pore volume was due to the exposure of lignin nuclei as a result of the formation of aromatic compounds with increasing final pyrolysis temperature.[46] Simultaneously, the increase in specific surface area indicated the development of an improving porous structure during the increasing heating process.[34] However, SSB600 showed the highest maximum Pb^{2+} adsorption capacity, although its specific surface area was lower than that of SSB700 (Fig. 1), which inferred that Pb^{2+} adsorption was also probably governed by other factors (such as precipitation).[47] It was generally acknowledged that the physical adsorption capacity mainly depended on the specific surface area itself, while chemical adsorption was related to the amounts of bonding sites. Notably, the results showed that there was no significant correlation between the Pb^{2+}

adsorption capacity and specific surface area of SSB400–700, which suggested that chemical adsorption also existed during the Pb^{2+} adsorption process by biochar (SSB400–700). For analyzing the vital chemical groups of SSB related to Pb^{2+} adsorption, the specific elements, functional groups, molecular structure, and surface electric charge were studied further.

The elemental composition of ss and SSB400–700 at different final pyrolysis temperatures is shown in Fig. 6a. The main elements of SSB were C, H, O, N, and S. With increasing, final pyrolysis temperature the contents of C, H, N, and S decreased, and the S contents in SSB were relatively low with a concentration below 2.00%. The ratio of H/C is a carbonization degree parameter that can be used to characterize the degree of aromaticity of the biochar.[48] The ratio of H/C decreased sharply with increasing pyrolysis temperature, which suggested a higher degree of aromatic condensation and stability of the biochar, developing with an enhanced degree of aromatic condensation. The ratio of C/N also decreased along with signal reduction of C and N elements with the pyrolysis temperature increasing from 400–700 °C, suggesting a greater loss of *N*-related functional groups in biochar or N depletion. The ratio of C/N was commonly used as a signal of the inorganic N releasing capacity of organic matters. Significantly, with the increase of final pyrolysis temperature, the contents of O, as well as O/C and (N + O)/C, decreased sharply from 27.2%, 0.818%, and 0.954% to 2.86%, 0.121%, and 0.185% respectively (Fig. 6a), which was the reason that the oxygen-containing groups of sewage sludge decomposed during the pyrolysis process. Therefore, compared to the initial sewage sludge, there should be less N in biochar. In particular, the molar ratio of O/C is widely characterized as the aromaticity of organic compounds. Generally, a smaller ratio indicated stronger aromaticity.[49] The decrease of O/C in SSB400–700 showed that more aromatic carbon structures and stronger stability formed at the higher temperature. And it was shown that nearly all the oxygen-containing groups decomposed, resulting in thorough carbonization over 700 °C.[50] Thus, it could be revealed clearly that the amounts of the oxygen-containing groups on the surface of SSB were the key factor for Pb^{2+} adsorption capacity by SSB.

Fig. 6b shows the FTIR spectra of SSB400–700. It comprised abundant hydrocarbon functional groups and oxygen-containing groups, including hydroxyl (with –OH stretching vibration peak at 3700–3200 cm^{-1}), carbonyl (with –C=O stretching vibration peak at 1755–1630 cm^{-1}), and ether (with –C–O–C– stretching vibration peak at 1053 cm^{-1}). This was coincident with previous studies,[51] and with increasing pyrolysis temperature, peaks of the hydroxyl group became weaker and weaker. The results suggested that Pb^{2+} adsorption performance by SSB400–700 was influenced by the hydrogen bonding between oxygen-containing functional groups and Pb^{2+}, and electrostatic interaction as well.[47]

The Raman spectra of SSB400–700 are shown in Fig. 6c, which are wildly utilized to identify the degree of graphitization and defect of carbonaceous materials.[52] There were obvious double peaks of SSB400–700 at around 1350–1370 cm^{-1} and 1600 cm^{-1}, among which 1350–1370 cm^{-1} was the characteristic band of amorphous carbon called the D-band, and around 1600 cm^{-1} was the characteristic peak of graphitic carbon called the G-band.[53] In general, the value of I_D/I_G is used to represent the disorder and defect degree of carbon materials; a higher I_D/I_G value means a higher disorder and defect degree of carbon materials, where I_D/I_G stands for the intensity of the D-band and G-band of carbon materials. After calculation, the value of I_D/I_G was 1.045 (SSB400), 1.052 (SSB500), 1.054 (SSB600), and 1.053 (SSB700), respectively. This indicated that the degree of disorder and defect of biochar improved along with increasing pyrolysis temperature (400–600 °C). The I_D/I_G value increases with the pyrolysis temperature, indicating that the proportion of defective and thickened aromatic structures increases, which is due to the hydrogenation aromatics and aromatic substances generated during the pyrolysis process. With increasing pyrolysis temperature, biochar mainly undergoes polycondensation reactions, and the compounds formed by the fracture of small molecular function groups on side chains were partially deposited on the surface of the biochar, forming defective and amorphous structures, which increased the disorder of biochar. It was reported that the defective structure of biochar can serve as the adsorption sites of the adsorbent,[54] and the I_D/I_G value had a positive correction with the Pb^{2+} removal efficiencies by

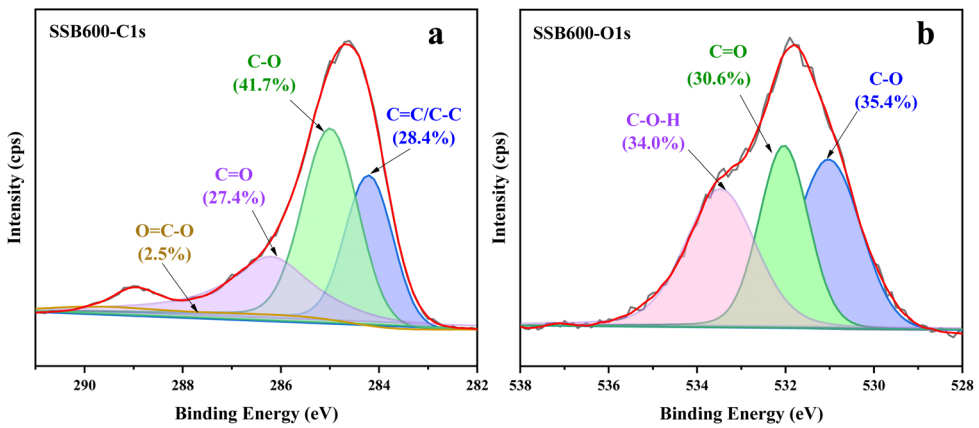

Fig. 7 High-resolution XPS spectra of C1s (a) and O1s (b) orbitals of SSB600.

Table 3 The peak area percentage of XPS spectra

Peak area percentage (%)							
	C1s				O1s		
	C=C/C–C	C–O	C=O	O=C–O	C–O	C=O	C–O–H
(eV)	285	286	287	290	531	532	533
SSB600	28.4	41.7	27.4	2.50	35.4	30.6	34.0

SSB400–700, as shown in Fig. 2. And this phenomenon suggested that the carbon atoms of SSB showed high defect levels, the surface was rich in oxygen-containing functional groups, and the SSB possessed a conjugate structure that was beneficial for π – electron coordination, hydrogen bonding, and electrostatic interaction to promote Pb^{2+} adsorption.

The relationship between the zeta potentials of SSB400–700 and pH is represented in Fig. 6d. The results suggested that the surface charge of SSB400–700 transitioned from positive to negative as the pH value rose from 4.45 to 8.72, with increasing pyrolysis temperature. The isoelectric point was 4.94, and when pH > 4.94, the hydroxyl groups were deprotonated, yielding a negative charge on the surface. Conversely, when pH < 4.94, these groups were protonated, resulting in a positive charge on the surface. Thus, it was suggested that the precipitates of Pb^{2+} could form above pH 4.94, and this result is approximate to that of Cheng[55] *et al.*, where the precipitates of Pb^{2+} formed at pH 5.50.

The XPS results suggested that the surface of SSB600 was rich in C, H, and O elements. The peak fitting results and peak area percentages for C1s and O1s in XPS spectra of SSB600 are provided in Fig. 7a and b. It revealed that the C1s spectra can be deconvoluted into four peaks centered at 285 eV, 286 eV, 287 eV, and 290 eV, which corresponded to C=C/C–C, C–O, C=O, and O=C–O, respectively. Similarly, the O1s spectra can also be deconvoluted into three peaks centered at 531 eV, 532 eV, and 533 eV, which represented C–O, C=O, and C–O–H, respectively (Table 3). A high percentage of oxygen-containing functional groups (C=O, C–O, and C–O–H) exhibited high chemical activity, which could also demonstrate the high Pb^{2+} adsorption capacity of SSB600, as shown in Fig. 2a. Furthermore, associated with the low ratio of O/C (Fig. 4), a large amount of C=C/C–C at 285 eV also suggested that there were more aromatic structures in SSB600. According to the peak area percentage of

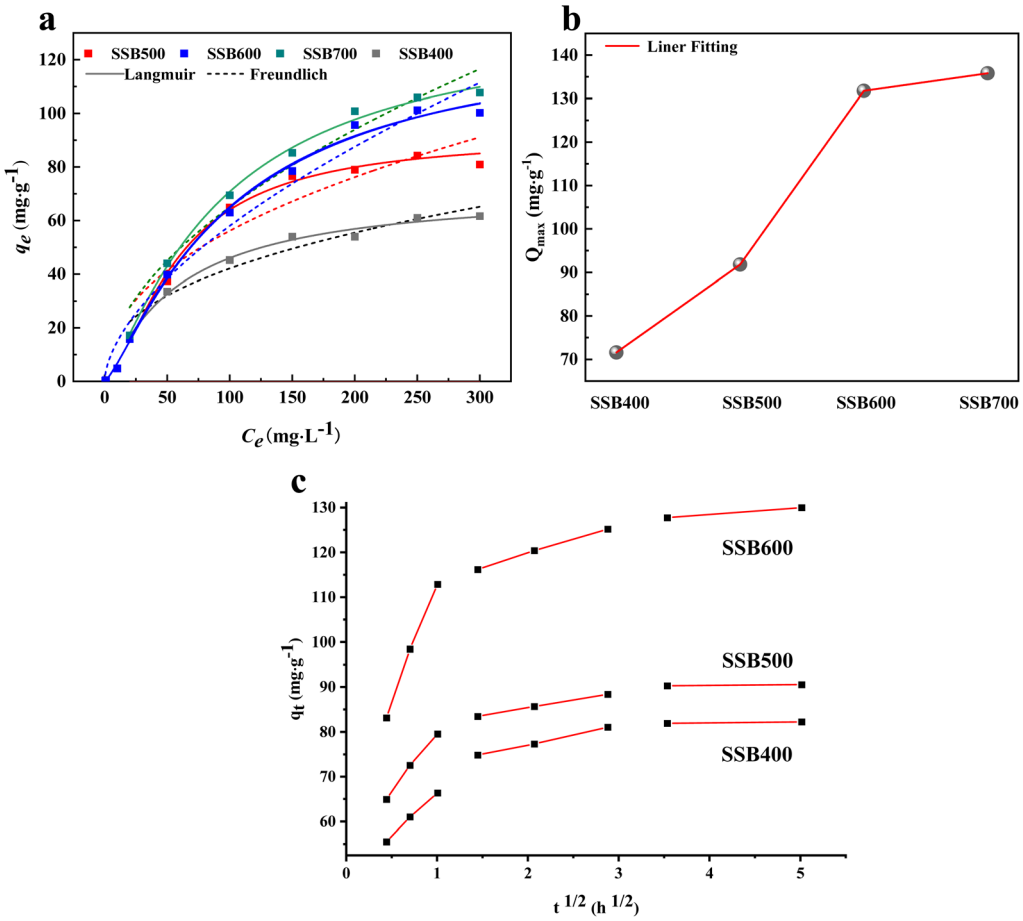

Fig. 8 Pb^{2+} adsorption isotherms of SSB400–700 with fittings by the Langmuir and Freundlich models (a); the maximum adsorption capacity (Q_m) derived from the Langmuir model (b); the intraparticle diffusion curve of Pb^{2+} by SSB400–600 (c) (adsorbent dosage = 1.00 g L^{-1}; initial pH = 5.00 ± 0.1; temperature = 25.0 °C; reaction time = 24 h; initial Pb^{2+} concentration range: 0.500, 1.00, 10.0, 20.0, 50.0, 100, 150, 200, 250, 300 mg L^{-1}).

Table 4 Isothermal model parameters for Pb^{2+} adsorption with SSB400–700

	Langmuir			Freundlich		
	Q_m (mg g^{-1})	K_L (L mg^{-1})	R^2	n	K_f (mg^{1-n} L^n g^{-1})	R^2
SSB400	71.6 ± 5.73	0.0110 ± 0.00572	0.987	0.400 ± 0.0521	6.76 ± 1.84	0.938
SSB500	91.8 ± 4.24	0.00200 ± 0.00123	0.989	0.440 ± 0.0871	7.36 ± 3.36	0.878
SSB600	131 ± 10.2	0.00300 ± 0.00220	0.997	0.595 ± 0.0000	4.74 ± 0.00	0.972
SSB700	136 ± 9.39	0.00149 ± 0.00149	0.995	0.530 ± 0.0646	5.63 ± 1.92	0.953

C═C/C–C and C–O at 285 eV (28.4%) and 286 eV (41.7%), it can be calculated that there were a lot of aromatic nuclei within the structure of SSB600. And a large amount of oxygen-containing functional groups connected with the aromatic structure, as confirmed in Fig. 6b. The oxygen-containing functional groups (such as –OH and C═O,) could form different complexes combined with Pb^{2+}, which was proved a contribution of oxygen-containing functional groups for Pb^{2+} adsorption.

3.3 The adsorption mechanism of SSB for Pb^{2+} removal

The Pb^{2+} adsorption isotherm curves of SSB400–700 that pyrolyzed at different temperature are shown in Fig. 8a, and detailed fitting parameters are listed in Table 4. The isotherm curves suggested that the Langmuir adsorption model ($R^2 > 0.987$) was more appropriately suitable than the Freundlich adsorption model ($R^2 > 0.878$), which proved that Pb^{2+} adsorption with SSB400–SSB700 was monolayer adsorption on the surface of SSB400–SSB700 and the active sites of SSB are relatively evenly distributed on the homogeneous surface.[56] And the theoretical adsorption capacities of SSB400–SSB700 for Pb^{2+} adsorption were 71.6 ± 5.73 mg g^{-1}, 91.8 ± 4.24 mg g^{-1}, 131 ± 10.2 mg g^{-1} and 136 ± 9.39 mg g^{-1}, respectively. And based on the high affinity suggested by the Langmuir model (Q_m = 131 ± 10.2 mg L^{-1}, K_L = 0.00300 ± 0.00220 L mg^{-1}, R^2 = 0.997) and the steeper initial slope of the isotherms, SSB600 still possessed strong binding sites effective at low concentrations. It can be found that with the increase of final pyrolysis temperature, the Pb^{2+} adsorption capacity of SSB showed an upward trend, and the adsorption capacity of SSB600 exhibited a higher Q_m increasing rate ($k_{SSB600–SSB700} = 0.0400 < k_{SSB500–SSB600} = 0.400 < k_{SSB400–SSB500} = 0.200$) (Fig. 8b) and adsorption affinity, which indicated the joint Pb^{2+} adsorption result of organic group complexation and precipitation.[34] Thus, a further Pb^{2+} adsorption analysis in following studies was investigated using SSB600. Previously, Liu *et al.*[34] used cotton straw to produce cotton straw-derived biochar *via* pyrolysis at 300–700 °C for Pb^{2+} adsorption (Pb^{2+} adsorption capacity: 49.7 mg g^{-1} < 131 mg g^{-1} in this study), among which a better Pb^{2+} removal performance was attained at 600 °C similarly. The reasons behind this phenomenon can be summarized as follows: biochar pyrolyzed at low temperature contained a variety of chemical components, including organic functional groups.[57] These organic groups exhibited a relatively low Pb^{2+} adsorption capacity. Furthermore, the low temperature resulted in slower mass transfer. In contrast, at higher pyrolysis temperature, the reduction of polar functional groups and the formation of inorganic salts contribute to the rapid adsorption of heavy metals. High temperature biochar also can develop more micropores, leading to a larger specific surface area,[58] which can enhance mass transfer efficiency. Consequently, adsorption equilibrium was achieved more quickly for biochar pyrolyzed at higher temperature. In addition, a higher temperature would lead to the deformation, collapse, and blockage of biochar micropores, resulting in thorough carbonization of biochar pyrolyzed over 700 °C, with only a slight increase in Pb^{2+} adsorption performance for SSB700.[59] This observation was consistent with this study; thus, SSB pyrolyzed at higher temperature, which possesses a greater surface area, enhanced superior microporosity and hydrophobicity, is conducive to Pb^{2+} adsorption.

This model was powerful for elucidating the rate-limiting steps and mass transfer mechanisms during the Pb^{2+} adsorption process. As shown in Fig. 8c, the Weber–Morris plots indicated that Pb^{2+} adsorption by SSB600 was a multi-stage process. The particle internal diffusion constants (k_1–k_3) were 31.6, 3.98, 0.492, respectively (Table S2). The initial stage was a rapid surface and boundary layer interaction, which determined the maximum adsorption rate. With the pyrolysis temperature increasing from 400–600 °C, the adsorption rates were increased from 20.9–31.6. The subsequent gradual stage was a gradual diffusion into the porous structure of SSB400–600. Crucially, the plots for the diffusion stage did not pass through the origin, indicating that intraparticle diffusion was involved but was not the sole rate-controlling step. This phenomenon provided strong kinetic evidence supporting the coexistence of multiple mechanisms (*e.g.*, complexation and ion exchange), which aligned with and reinforced the multi-mechanism model proposed from equilibrium studies. The final plateau signified the equilibrium stage and saturation of available adsorption sites.

In addition to the parameters of the Langmuir and Freundlich models fitted to the Pb^{2+} adsorption data of SSB400–700, the standard errors of the parameters are also summarized in Table 4. First, the high determination coefficient ($R^2 \geq 0.987$) of the Langmuir model and the relatively low standard errors associated with the estimated parameters (such as Q_m) jointly indicated that the Langmuir model could reliably and robustly describe the adsorption isotherm. This further confirmed the conclusion that monolayer adsorption occurs on a relatively uniform surface. Notably, the relative error of Q_m was relatively controllable, which showed a sharp increasing trend with pyrolysis temperature. The relative errors of Q_m ranged from ±4.60% to ±8.00% at 400 °C, 500 °C, and 700 °C, indicating the

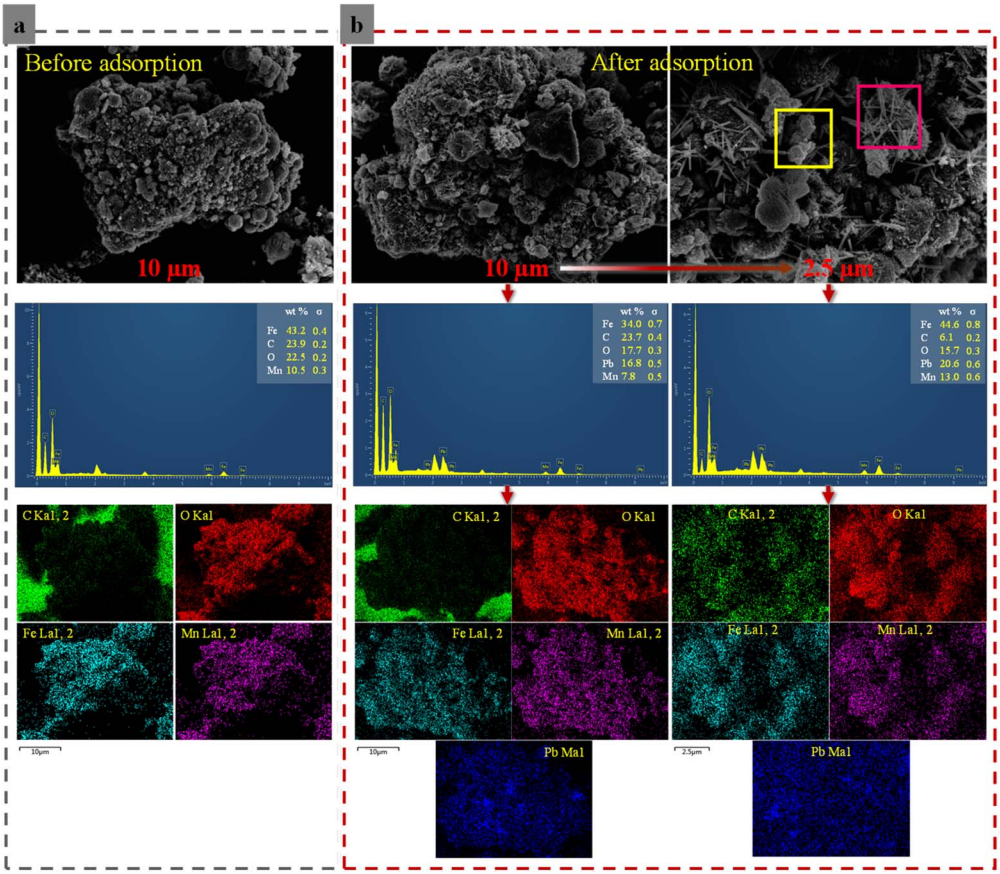

Fig. 9 SEM-EDS spectra and elemental mapping images of SSB600 before (a) and after (b) Pb^{2+} adsorption (SEM magnification: 2.00k× and 5.00k×); the Pb-loaded sample was obtained from adsorption experiments at an initial Pb^{2+} concentration of 100 mg L^{-1}, adsorbent dosage: 1.00 g L^{-1}, pH: 5.00 ± 0.1, 25.0 °C, reaction time: 24 h.

reliability of Langmuir model's prediction of saturated adsorption capacity. And the optimal SSB600 exhibited a larger relative error in Q_m (±11.9%), which suggested a greater heterogeneity in the availability or energy distribution of its adsorption sites, likely stemming from the complex interplay between carbonization and mineral formation at 600 °C. The Langmuir constant (K_L), indicating adsorption affinity, was generally small (ranging from 0.00100 to 0.0110), which carried a large uncertainty (relative error: 52.0%–100% for SSB400–700). This was common in the adsorption process at low pollutant concentrations. And in the Freundlich model, the heterogeneity factor, n, was less than 1 for SSB400–700, confirming favorable adsorption. And the highest value of SSB600 ($n = 0.550 \pm 0.0680$) aligned with the Langmuir model fitting, reinforcing the notion of its highly heterogeneous surface at 600 °C. Notably, the Freundlich intensity parameter K_f showed large standard errors (relative error: 27.0%–46.0%), indicating that it was unstably reliable to compare adsorption strength across diverse biochars. This error analysis underscored that compared to the Freundlich model, the Langmuir model offered a more physically plausible and stable fitting (monolayer adsorption) of the dominant adsorption process.

Fig. 9 illustrates the surface morphology and elemental composition of SSB600 before and after Pb^{2+} adsorption. Before adsorption, the SSB600 surface was rough with a well-developed porous structure, which contained elements of C, O, Fe, and Mn (Fig. 9a). And after Pb^{2+} adsorption, EDS and mapping analysis revealed that Pb^{2+} was successfully and uniformly adsorbed on the surface of SSB600. The Pb elements on the SSB600 surface are spatially coincident with Fe and Mn elements, which suggested that the Fe and Mn oxides on the surface of SSB600 likely facilitated Pb^{2+} adsorption. It has reported that Fe and Mn oxides on biochar played a crucial role in the adsorption of heavy metals, as they can form metal–organic complexes.[60,61] Based on the Pb^{2+} adsorption experiment conducted under acidic conditions (initial pH 5)in this study, it was proposed that Fe and Mn oxides can complex with Pb^{2+}, leading to the formation of Fe–Pb oxide crystals and Mn–Pb oxide crystals. As shown in Fig. 9b, needle-like and rod-shaped crystals, as well as blocky grayish-white particles, appeared on the surface of SSB600. These were uniformly distributed in a flower-like or radiating shape and agglomerated or embedded on the SSB600 surface. This observation confirmed the presence of Fe–Pb oxide crystals and Mn–Pb oxide crystals. This proved that precipitation was one of the primary Pb^{2+} adsorption mechanisms by SSB600.

During the Pb^{2+} adsorption process by SSB (for example SSB600), the contribution of diverse mechanisms to the Pb^{2+}

Table 5 The contribution percentage of Pb^{2+} adsorption mechanisms by SSB600

SSB600	Complexation	Cation exchange	π–electron coordination	Precipitation
Adsorption amounts (mg g^{-1})	11.1	10.8	5.40	0.900
Contribution percentage (%)	39.2	38.3	19.2	3.30

adsorption could be calculated. The contributions of precipitation (q_1), cation exchange (q_2), complexation (q_3), and π–electron coordination (q_4) are shown in Table 5. Precipitation (q_1) and cation exchange (q_2) contributed 41.6% in the total adsorption capacity, complexation (q_3) accounted for 39.2%, and π–electron coordination (q_4) was 19.2%, respectively. First, the grey crystals showed in SEM could prove the precipitation effect by Fe and Mn oxides with Pb^{2+}. Besides, SSB also had the inorganic cations such as K^+, Ca^{2+}, and Na^+, which could realize Pb^{2+} removal from wastewater by the cation exchange reaction.[62] In addition, oxygen-containing functional groups (–OH and C=O) could combine with Pb^{2+} by the complexation effect, and $Pb(OH)_2$ could also be formed as a complex. Moreover, Pb^{2+} permitted for a Pb^{2+}–π coordination between the electron donor of the Pb^{2+} and the π–electron acceptor in the aromatic structure of SSB600.

In Table S3, the properties, Pb^{2+} adsorption capacity and adsorption mechanisms of SSB600 were compared with biochars derived from similar or different materials (*e.g.*, sewage sludge, Douglas fir, peanut shell, and commercial activated carbon) reported in recent studies. First, a trend was observed in which the yields of SSB decreased as the pyrolysis temperature increased from 400–700 °C (Fig. 3b). This result was highly consistent with those of similar sludge pyrolysis studies and was significantly higher than that of biomass raw materials mainly composed of cellulose (Table S1) and plants (Table S3).

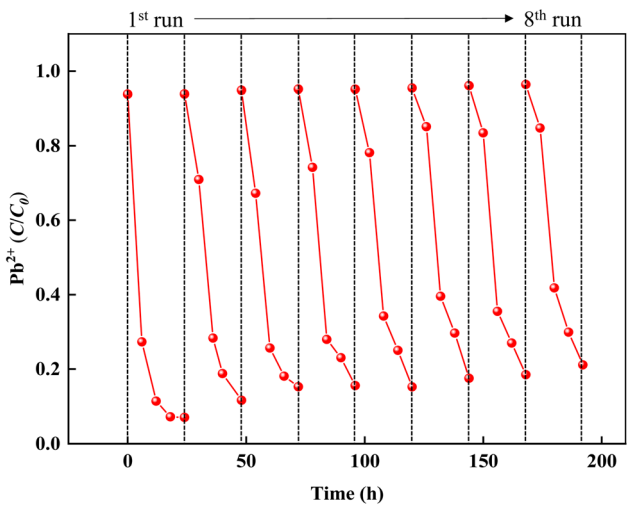

Fig. 10 The recycle experiment for Pb^{2+} adsorption by SSB600 (adsorption conditions of per cycle: adsorbent dose = 1.00 g L^{-1}, initial Pb^{2+} concentration = 100 mg L^{-1}, volume = 20.0 mL, pH = 5.00 ± 0.1, temperature = 25.0 °C, reaction time = 24 h, regenerant = 0.100 mol L^{-1} HNO_3).

This consistency reasonably reflected the characteristics of high ash contents (inorganic minerals) of municipal sewage sludge as raw materials, which remained as a substrate during the pyrolysis process and resulted in a relatively higher yield. In addition, regarding the final pyrolysis temperature corresponding to the optimal Pb^{2+} adsorption performance, the reported studies indicated that the optimal temperature for sludge-based biochar was typically concentrated in the medium–high temperature range (400–600 °C). And this study found that the material prepared at 600 °C had the highest Pb^{2+} adsorption capacity (132 mg g^{-1}), which precisely reflected that the optimal pyrolysis temperature was influenced by the specific raw material properties, the pyrolysis process, and the evaluation system. While the specific surface area of SSB600 was moderate compared to some plant-derived biochars, its superior adsorption capacity could be attributed to the synergistic effect of its higher pH (favoring precipitation), abundant mineral content (providing ion exchange and precipitation sites), and complex surface functional groups. This highlighted the unique advantage of municipal sewage sludge as a raw material for producing biochar with multifunctional adsorption mechanisms.

3.4 The leaching risk analysis of DOM in SSB

First, the total amounts of key heavy metals (Cd, Cr, Cu, Ni, Pb and Zn) in DOM600 were analyzed in the prepared biochar (SSB600), as shown in Table S4. The contents of Cd, Cr, Cu, Ni, Pb and Zn in all samples were far below the strict limit values of the sludge pollutant control standards (<0.001 ± 0.000), which indicated that the total amounts of heavy metals in DOM600 was controllable in terms of risk under the pyrolyzing process in this study. Besides, it was found that the sample contained various organic compounds in DOM600, including phenols, amides, polycyclic aromatic hydrocarbons, *etc.*, which indicated that at higher pyrolysis temperature, the concentration of organic compounds in SSB was at a relatively low level. Furthermore, the microbial toxicity of DOM600 release (leaching simulation) in SSB was studied by the luminescence inhibition experiment using *Vibrio fischeri*. The results indicated that the ecological toxicity of DOM600 in SSB was low (fluorescence inhibition efficiency: 8.60%), which provided a biological basis for risk assessment.

In summary, it has been demonstrated that the leaching risks of heavy metals and soluble organic components of DOM600 released from SSB were relatively low under the present pyrolysis conditions. This has confirmed the safety of sludge biochar as an adsorbent in practical technical applications.

3.5 The recycling performance of SSB600 for Pb^{2+} removal

To enable the application of SSB600 in practical adsorption, the adsorbing stability of SSB600 was further investigated. The results are shown in Fig. 10, SSB600 showed high adsorbing activity, with Pb^{2+} adsorption by SSB600 exceeding 79.0% after being recycled 8 times, indicating that SSB600 had good adsorbing capacity and stability.

4 Conclusions

This study systematically demonstrated that pyrolysis temperature was a critical factor governing the physicochemical properties of sewage sludge-derived biochar (SSB) and its effectiveness for Pb^{2+} remediation. SSB produced at 600 °C (SSB600) emerged as the optimal adsorbent, possessing a well-developed porous structure, high specific surface area, and abundant surface functional groups, which conferred a maximum Pb^{2+} adsorption capacity of 131 ± 10.2 mg g^{-1}. The adsorption process was best described by the Langmuir isotherm and involved a multi-stage kinetic mechanism. Importantly, SSB600 exhibited strong practical potential, retaining high adsorption performance across a wide pH range and in the presence of common competing ions. The adsorption mechanism was quantitatively deciphered, revealing synergistic contributions from complexation, cation exchange, π–electron interaction, and precipitation. Furthermore, SSB600 showed excellent regenerability over multiple cycles and effective removal at environmentally relevant concentrations, with its environmental safety validated by standard leaching tests. These findings provided a pyrolysis temperature-guided strategy for transforming sewage sludge into a high-performance, stable, and reusable adsorbent for heavy metal-contaminated water treatment.

5 Perspectives for future research

Although this work offered a systematic understanding of the influence of final pyrolysis temperature on the physicochemical properties, Pb^{2+} adsorption performance, and underlying mechanisms of SSB, several limitations of the present study should be acknowledged, as they provided important direction for future research. The experiments were conducted under batch conditions using simplified synthetic aqueous solutions, which do not reflect the hydrodynamic behavior of continuous-flow systems or the potential interference from more co-existing ions commonly present in real wastewater. Furthermore, the long-term stability and potential leaching risks associated with SSB would need further investigation.

To address these limitations, future studies should prioritize the following aspects: (1) pilot-scale validation through dynamic column experiments to derive practical engineering parameters; (2) assessment of adsorption selectivity and efficiency in complex, real Pb^{2+}-containing wastewater matrices; (3) development of strategies for heavy metal recovery from saturated biochar and its subsequent regeneration, thereby supporting circular economy principles; and (4) comprehensive life cycle analysis (LCA) and techno-economic evaluations to determine the environmental sustainability and economic viability of the adsorption process. Additionally, extending this pyrolysis optimization strategy to the treatment of other contaminants was strongly recommended.

Author contributions

Rui Zhao – conceptualization, investigation, data analysis, writing – review & editing. Xin Li – validation, supervision, funding acquisition, writing – review & editing. Xiaoxin Jiang – conceptualization, investigation, data analysis, writing – review & editing. Guangzhi Wang – validation, supervision, writing – review & editing. Guoren Xu – validation, supervision, writing – review & editing. Sai Qi – investigation, data analysis. Guoke Zhang – data analysis, writing – review & editing.

Conflicts of interest

The authors declare no competing financial interests. We declare that we have no financial and personal relationships with other people or organizations that can inappropriately influence our work, there is no professional or other personal interest of any nature or kind in any product, service and/or company that could be construed as influencing the position presented in, or the review of, the manuscript entitled “Pyrolysis temperature dependence of Pb^{2+} removal by sewage sludge biochar: characteristic evaluation and adsorption performance”.

Data availability

The authors confirm that the data supporting the findings of this study are available within the article.

Supplementary information (SI): Fig. S1: The amount of Pb^{2+} adsorbed by SSB600 and equilibrium pH at different initial pH (2.00–6.00) and ionic strength (Na^+, NO_3^-), Fig.S2: The mapping of SSB600, Fig.S3: Adsorption/desorption isotherm and pore size distribution at nitrogen atmosphere of SS, SSB400-700, Table S1: The yields of biochar pyrolyzing by various agricultural biomass, Table S2: The parameters of Weber-Morris's intraparticle diffusion model for Pb^{2+} adsorption by SSB, Table S3: the comparison of properties, Pb^{2+} adsorption performance, and mechanisms between other biochars and SSB600, Table S4: the composition of DOM in SSB600. See DOI: https://doi.org/10.1039/d5va00202h.

Acknowledgements

The authors greatly acknowledge the financial support from the project of Science Foundation of National Engineering Research Center for Safe Disposal and Resources Recovery of Sludge (Harbin Institute of Technology, Grant No Z2024A006), National Key Research and Development Program of China (Grant No 2019YFC1906501, 2018YFC1901100), and Open Project of State Key Laboratory of Urban-rural Water Resources and Environment (Harbin Institute of Technology, Grant No MS202529).

References

1 W. Zhang, S. Mao, H. Chen, L. Huang and R. Qiu, Pb(II) and Cr(VI) sorption by biochars pyrolyzed from the municipal wastewater sludge under different heating conditions, *Bioresour. Technol.*, 2013, **147**, 545–552.

2 H. Kominko, K. Gorazda and Z. Wzorek, Effect of sewage sludge-based fertilizers on biomass growth and heavy metal accumulation in plants, *J. Environ. Manage.*, 2022, **305**, 114417.

3 Y. V. Dubinin, N. A. Yazykov, A. P. Lyulyukin and V. A. Yakovlev, Combustion of sewage sludge in a fluidized bed of catalyst: from laboratory to the pilot plant, *Waste Manage.*, 2025, **204**, 114944.

4 N. K. Soni, K. Yadav, P. Prabhansu and P. V. Bhale, Synthesis and characterization of sewage sludge biochar toward adsorptive removal of pollutants for sustainability: a review, *J. Therm. Anal. Calorim.*, 2025, **150**, 3967–3989.

5 X. Zhang, B. Zhao, H. Liu, Y. Zhao and L. Li, Effects of pyrolysis temperature on biochar's characteristics and speciation and environmental risks of heavy metals in sewage sludge biochars, *Environ. Technol. Innovation*, 2022, **26**, 102288.

6 V. Pelagalli, M. Langone, S. Matassa, M. Race, R. Tuffi, S. Papirio, P. N. L. Lens, M. Lazzazzara, A. Frugis, L. Petta and G. Esposito, Pyrolysis of municipal sewage sludge: challenges, opportunities and new valorization routes for biochar, bio-oil, and pyrolysis gas, *Environ. Sci.:Water Res. Technol.*, 2024, **10**, 2282–2312.

7 D. Zhong, Y. Jiang, Z. Zhao, L. Wang, J. Chen, S. Ren, Z. Liu, Y. Zhang, D. C. W. Tsang and J. C. Crittenden, pH Dependence of Arsenic Oxidation by Rice-Husk-Derived Biochar: Roles of Redox-Active Moieties, *Environ. Sci. Technol.*, 2019, **53**, 9034–9044.

8 Y. Zhao, X. Li, Y. Li, H. Bao, J. Xing, Y. Zhu, J. Nan and G. Xu, Biochar Acts as an Emerging Soil Amendment and Its Potential Ecological Risks: A Review, *Energies*, 2022, **16**, 1–32.

9 V. Karthik, S. Periyasamy, S. Dharneesh, G. K. Duvakeesh, D. G. Gizaw and T. Vijayashankar, Biochar as a Sustainable Adsorbent for Heavy Metal Removal From Polluted Waters: A Comprehensive Outlook, *J Chem*, 2024, **2024**, 8217730.

10 I. R. Chowdhury, S. Chowdhury, M. A. J. Mazumder and A. Al-Ahmed, Removal of lead ions (Pb(2+)) from water and wastewater: a review on the low-cost adsorbents, *Appl Water Sci*, 2022, **12**, 185.

11 S. Satyam and S. Patra, Innovations and challenges in adsorption-based wastewater remediation: A comprehensive review, *Heliyon*, 2024, **10**, e29573.

12 D. Lukić, V. Vasić, J. Živančev, I. Antić, S. Panić, M. Petronijević and N. Đurišić-Mladenović, Adsorption Performance Assessment of Agro-Waste-Based Biochar for the Removal of Emerging Pollutants from Municipal WWTP Effluent, *Molecules*, 2025, **30**, 4803.

13 B. Zhao, D. O'Connor, J. Zhang, T. Peng, Z. Shen, D. C. W. Tsang and D. Hou, Effect of pyrolysis temperature, heating rate, and residence time on rapeseed stem derived biochar, *J. Cleaner Prod.*, 2018, **174**, 977–987.

14 H. Huang, N. G. Reddy, X. Huang, P. Chen, P. Wang, Y. Zhang, Y. Huang, P. Lin and A. Garg, Effects of pyrolysis temperature, feedstock type and compaction on water retention of biochar amended soil, *Sci. Rep.*, 2021, **11**, 7419.

15 S. R. Naqvi, R. Tariq, M. Shahbaz, M. Naqvi, M. Aslam, Z. Khan, H. Mackey, G. McKay and T. Al-Ansari, Recent developments on sewage sludge pyrolysis and its kinetics: Resources recovery, thermogravimetric platforms, and innovative prospects, *Comput. Chem. Eng.*, 2021, **150**, 107325.

16 K. Zhao, C. Si, P. Zhang and Y. Cui, Thermal gradient-driven heavy metal speciation and risk evolution in municipal and industrial sludge: a 300–700 °C pyrolysis perspective, *RSC Adv.*, 2025, **15**, 43932–43940.

17 M. Pahnila, A. Koskela, P. Sulasalmi and T. Fabritius, A Review of Pyrolysis Technologies and the Effect of Process Parameters on Biocarbon Properties, *Energies*, 2023, **16**, 6936.

18 A. Iurchenkova, A. Kobets, Z. Ahaliabadeh, J. Kosir, E. Laakso, T. Virtanen, V. Siipola, J. Lahtinen and T. Kallio, The effect of the pyrolysis temperature and biomass type on the biocarbons characteristics, *ChemSusChem*, 2024, **17**, e202301005.

19 Y. Wei, J. Ma, K. Liu, S. Zhang and J. Wang, Biochar-Based Remediation of Heavy Metal-Contaminated Soils: Mechanisms, Synergies, and Sustainable Prospects, *Nanomaterials*, 2025, **15**, 1487.

20 D. Wang, L. Huang, H. Fang, S. Li, G. Wang, S. Zhou, R. Zhao and X. Sun, Activated carbon fibers functionalized with superhydrophilic coated pDA/TiO2/SiO2 with photoluminescent self-cleaning properties for efficient oil-water separation, *J. Hazard. Mater.*, 2024, 465.

21 C. Zhao, X. Liu, A. Chen, J. Chen, W. Lv and X. Liu, Characteristics evaluation of bio-char produced by pyrolysis from waste hazelnut shell at various temperatures, *Energy Sources, Part A*, 2020, 1–11, DOI: 10.1080/15567036.2020.1754530.

22 J. A. Antonangelo, S. Culman and H. Zhang, Comparative analysis and prediction of cation exchange capacity *via* summation: influence of biochar type and nutrient ratios, *Front. Soil Sci*, 2024, 4–2024.

23 W. Ahmad, R. D. Alharthy, M. Zubair, M. Ahmed, A. Hameed and S. Rafique, Toxic and heavy metals contamination assessment in soil and water to evaluate human health risk, *Sci. Rep.*, 2021, **11**, 1–12.

24 L. Irving, Adsorption of gases on glass, mica and platinum, *J. Am. Chem. Soc.*, 1918, **40**, 1361–1403.

25 P. He, Y. Zhang, X. Zhang and H. Chen, Diverse zeolites derived from a circulating fluidized bed fly ash based geopolymer for the adsorption of lead ions from wastewater, *J. Cleaner Prod.*, 2021, **312**, 1–10.

26 K. H. Chu, M. A. Hashim, M. H. Zawawi and J.-C. Bollinger, The Weber–Morris model in water contaminant adsorption: Shattering long-standing misconceptions, *J. Environ. Chem. Eng.*, 2025, **13**, 117266.

27 C. Li, J.-i. Hayashi, Y. Sun, L. Zhang, S. Zhang, S. Wang and X. Hu, Impact of heating rates on the evolution of function groups of the biochar from lignin pyrolysis, *J. Anal. Appl. Pyrolysis*, 2021, **155**, 105031.
28 A. Kritikaki, V. Karmali, D. Vathi, G. Bartzas and K. Komnitsas, Advanced Characterization of Biochars Produced from Three Different Organic-based Feedstocks and their Potential Applications, *Circ. Econ. Sustainability*, 2025, **5**, 7465–7488, DOI: 10.1007/s43615-025-00580-w.
29 D. S. Hansen, A. E. Turcios, A. M. Klamt, C. Wieth, K. Reitzel, M. H. Thomsen and J. Papenbrock, Characterization of biochar produced from sewage sludge and its potential use as a substrate and plant growth improver, *J. Environ. Manage.*, 2023, **348**, 119271.
30 Z. Zhang, L. Cheng, Q. Hu and Z. Hu, Influence of pyrolysis temperature on speciation, leaching and environmental risk assessment of heavy metals in biochar and bio-oil from pyrolysis of wet sewage sludge, *Biomass Convers. Biorefin.*, 2025, **15**, 19363–19376.
31 J. Kujawska, E. Wojtaś and B. Charmas, Biochar Derived from Sewage Sludge: The Impact of Pyrolysis Temperature on Chemical Properties and Agronomic Potential, *Sustainability*, 2024, **16**, 8225.
32 X. Zhang, P. Zhang, X. Yuan, Y. Li and L. Han, Effect of pyrolysis temperature and correlation analysis on the yield and physicochemical properties of crop residue biochar, *Bioresour. Technol.*, 2020, **296**, 122318.
33 H. Yuan, T. Lu, H. Huang, D. Zhao, N. Kobayashi and Y. Chen, Influence of pyrolysis temperature on physical and chemical properties of biochar made from sewage sludge, *J. Anal. Appl. Pyrolysis*, 2015, **112**, 284–289.
34 Z. Wang, J. Xu, D. Yellezuome and R. Liu, Effects of cotton straw-derived biochar under different pyrolysis conditions on Pb (II) adsorption properties in aqueous solutions, *J. Anal. Appl. Pyrolysis*, 2021, **157**, 1–8.
35 W. Shi, W. Lian, S. Tian, X. Gong, Q. Yu, Z. Guo, X. Zhang, B. Ma, R. Bian, J. Zheng, K. Cheng and G. Pan, A review of agronomic and environmental properties of inorganic compounds in biochars, *Curr. Res. Environ. Sustain*, 2023, **5**, 100226.
36 C. Li, W. Shao, Q. Dong, L. Ji, Q. Li, A. Zhang, C. Chen and W. Yao, The Effects of Acid-Modified Biochar and Biomass Power Plant Ash on the Physiochemical Properties and Bacterial Community Structure of Sandy Alkaline Soils in the Ancient Region of the Yellow River, *Sustainability*, 2024, **16**, 8909.
37 N. Bolan, A. K. Sarmah, S. Bordoloi, S. Bolan, L. P. Padhye, L. Van Zwieten, P. Sooriyakumar, B. A. Khan, M. Ahmad, Z. M. Solaiman, J. Rinklebe, H. Wang, B. P. Singh and K. H. M. Siddique, Soil acidification and the liming potential of biochar, *Environ. Pollut.*, 2023, **317**, 120632.
38 R. Janu, V. Mrlik, D. Ribitsch, J. Hofman, P. Sedláček, L. Bielská and G. Soja, Biochar surface functional groups as affected by biomass feedstock, biochar composition and pyrolysis temperature, *Carbon Resour. Convers.*, 2021, **4**, 36–46.
39 J. Yao, X. Wang, M. Hong, H. Gao and S. Zhao, Response of soil pH to biochar application in farmland across China: a meta-analysis, *PeerJ*, 2025, **13**, e19400.
40 M. J. Romero-Guzmán, V. Petris, S. De Chirico, V. di Bari, D. Gray, R. M. Boom and C. V. Nikiforidis, The effect of monovalent (Na+, K+) and divalent (Ca2+, Mg2+) cations on rapeseed oleosome (oil body) extraction and stability at pH 7, *Food Chem.*, 2020, **306**, 125578.
41 J. Xu, X. Wang, W. Kang and W. Zhang, Study on the adsorption of Pb2+ in aqueous solution by alkali modified wheat bran, *Sci. Rep.*, 2025, **15**, 21236.
42 H. Xu, Q. Zhou, T. Yan, X. Jia, D. Lu, Y. Ren and J. He, Enhanced removal efficiency of Cd2+ and Pb2+ from aqueous solution by H3PO4–modified tea branch biochar: Characterization, adsorption performance and mechanism, *J. Environ. Chem. Eng.*, 2024, **12**, 112183.
43 H. Xie, H. Ao, L. Xu, S. Ao, T. Zhang, W. Li and Y. Yang, Quantum chemical DFT-based adsorption mechanism of Pb(II) on a modified biochar, *Biomass Convers. Biorefin.*, 2024, **14**, 13547–13562.
44 H. L. Fuhua Chang, Preparation of high-efficient $KMnO_4$ modified biochar for heavy metal removal from municipal wastewater, *Arabian J. Chem.*, 2024, **17**, 1–9.
45 X. Zhou, X. Liu, L. Sun, X. Jia, F. Tian, Y. Liu and Z. Wu, Prediction of Biochar Yield and Specific Surface Area Based on Integrated Learning Algorithm, *Journal of Carbon Research*, 2024, **10**, 10.
46 H. Rennhofer, J. Köhnke, J. Keckes, J. Tintner, C. Unterweger, T. Zinn, K. Deix, H. Lichtenegger and W. Gindl-Altmutter, Pore Development during the Carbonization Process of Lignin Microparticles Investigated by Small Angle X-ray Scattering, *Molecules*, 2021, **26**, 2087.
47 R.-h. Liang, Y. Li, L. Huang, X.-d. Wang, X.-x. Hu, C.-m. Liu, M.-s. Chen and J. Chen, Pb2+ adsorption by ethylenediamine-modified pectins and their adsorption mechanisms, *Carbohydr. Polym.*, 2020, **234**, 115911.
48 L. Wei, Y. Huang, L. Huang, Y. Li, Q. Huang, G. Xu, K. Müller, H. Wang, Y. S. Ok and Z. Liu, The ratio of H/C is a useful parameter to predict adsorption of the herbicide metolachlor to biochars, *Environ. Res.*, 2020, **184**, 109324.
49 J. Ippolito, L. Cui, C. Kammann, N. Wrage-Mönnig, J. Estavillo, T. Fuertes-Mendizábal, M. L. Cayuela, G. Sigua, J. Novak, K. Spokas and N. Borchard, Feedstock choice, pyrolysis temperature and type influence biochar characteristics: a comprehensive meta-data analysis review, *Biochar*, 2020, **2**, 421–438.
50 H. Dang, R. Xu, J. Zhang, M. Wang, L. Ye and G. Jia, Removal of oxygen-containing functional groups during hydrothermal carbonization of biomass: Experimental and DFT study, *Energy*, 2023, **276**, 127436.
51 C. Yang, Z. Wan, H. Wang, J. Zang, X. Wang, F. Yang, G. Zhang, W. Zhao, L. Liu, Y. Liu, W. Dong, W. Xie, Y. Tang and W. Wang, Temperature-Dependent Adsorption Process of Neonicotinoid Insecticide Nitenpyram by

Sawdust Biochar: Mechanism and Theoretical Simulation, *ACS Agric. Sci. Technol.*, 2023, **4**, 22–33.

52 J. Tu, X. Wang, L. Jiang, B. Zhang, M. Wang, Y. Li and S. Jiao, Efficient graphitization conversion strategies of low-value carbonaceous resources into advanced graphitic carbons, *Chem. Eng. J.*, 2025, **505**, 159472.

53 D. Ouyang, Y. Chen, J. Yan, L. Qian, L. Han and M. Chen, Activation mechanism of peroxymonosulfate by biochar for catalytic degradation of 1,4-dioxane: Important role of biochar defect structures, *Chem. Eng. J.*, 2019, **370**, 614–624.

54 D. Bao, Z. Li, R. Tang, C. Wan, C. Zhang, X. Tan and X. Liu, Metal-modified sludge-based biochar enhance catalytic capacity: Characteristics and mechanism, *J. Environ. Manage.*, 2021, 284.

55 S. Cheng, W. Meng, B. Xing, C. Shi, Q. Wang, D. Xia, Y. Nie, G. Yi, C. Zhang and H. Xia, Efficient removal of heavy metals from aqueous solutions by Mg/Fe bimetallic oxide-modified biochar: Experiments and DFT investigations, *J. Cleaner Prod.*, 2023, **403**, 1–12.

56 W. Shenjin, L. Xiaoxi, Z. Chenyang, H. Wenjihao, L. Yaochi, F. Xinzhuang, Y. Jun and S. Wei, Adsorption and selective mechanism of Pb2+and Cd2+on the surface of calcined modified attapulgite, *Sep. Purif. Technol.*, 2025, **353**, 128377.

57 H. Lin, J. Xie, Y. Dong, J. Liu, K. Meng and Q. Jin, A complete review on the surface functional groups in pyrolyzed biochar and its interaction mechanism with heavy metal in water, *J. Environ. Chem. Eng.*, 2025, **13**, 116681.

58 S. Liu, S. Peng, B. Zhang, B. Xue, Z. Yang, S. Wang and G. Xu, Effects of biochar pyrolysis temperature on thermal properties of polyethylene glycol/biochar composites as shape-stable biocomposite phase change materials, *RSC Adv.*, 2022, **12**, 9587–9598.

59 I. G. Edeh, O. Masek and F. Fusseis, 4D structural changes and pore network model of biomass during pyrolysis, *Sci. Rep.*, 2023, **13**, 22863.

60 L. Zhang, X. Liu, X. Huang, W. Wang, P. Sun and Y. Li, Adsorption of Pb(2+) from aqueous solutions using Fe-Mn binary oxides-loaded biochar: kinetics, isotherm and thermodynamic studies, *Environ. Technol.*, 2019, **40**, 1853–1861.

61 S. Liu, J. Huang, W. Zhang, L. Shi, K. Yi, C. Zhang, H. Pang, J. Li and S. Li, Investigation of the adsorption behavior of Pb(II) onto natural-aged microplastics as affected by salt ions, *J. Hazard. Mater.*, 2022, **431**, 128643.

62 S. Cheng, S. Zhao, H. Guo, B. Xing, Y. Liu, C. Zhang and M. Ma, High-efficiency removal of lead/cadmium from wastewater by MgO modified biochar derived from crofton weed, *Bioresour. Technol.*, 2022, 343.